Applied Catalysis B: Environmental 217 (2017) 540–550

Contents lists available at ScienceDirect

Applied Catalysis B: Environmental

journal homepage: www.elsevier.com/locate/apcatb

Development of Carbon-ZrO_2 composites with high performance as visible-light photocatalysts

Esther Bailón-García, Abdelhakim Elmouwahidi, Francisco Carrasco-Marín, Agustín F. Pérez-Cadenas, Francisco J. Maldonado-Hódar*

Research Group in Carbon Materials, Inorganic Chemistry Department, Faculty of Sciences, University of Granada, Campus Fuentenueva s/n, 18071, Granada, Spain

ARTICLE INFO

Article history:
Received 18 February 2017
Received in revised form 29 May 2017
Accepted 30 May 2017
Available online 4 June 2017

Keywords:
Carbon-ZrO_2 composites
Visible light photocatalysts
Band-gap reduction
Total mineralization
Toxicity reduction

ABSTRACT

Mesoporous carbon-ZrO_2 composites (CZrX) were successfully synthesized by a direct sol-gel procedure. A large battery of experimental techniques is applied for sample characterization. ZrO_2 nanoparticles were homogeneously distributed on the carbon supports and stabilized in the cubic phase. The interactions between organic-inorganic phases determine the formation of non-stoichiometric ZrOx oxides, the reduction of the ZrO_2 band-gap values and the charge carriers' recombination, favouring the absorbance of visible light and the photocatalytic behaviour. The total mineralization of the dye and the simultaneous reduction of the toxicity are achieved.

1. Introduction

Environmental photocatalysis is an advanced technology that employs photon excited semiconductors to remove pollutants via redox reactions. The photocatalytic efficiency in semiconductors is greatly affected by the quick recombination of charge carriers. The electron–hole pairs generated in the semiconductor by irradiation can be easily recombined and consequently, a loss of activity can be observed. Obviously, an ideal photocatalyst should be: (i) photoactive; (ii) biologically and chemically inert; (iii) active under visible and/or near-UV light; (iv) inexpensive and (v) photostable. TiO_2 semiconductor satisfies the most of these criteria and so that is one of the most used photocatalysts [1]. However, only 3–5% of UV in solar spectrum can be absorbed by pure TiO_2 due to the wide band gap (3.2 eV of anatase and 3.0 eV of rutile), which greatly restricts its photocatalytic applications in the visible-light range [2,3].

Trying to improve the efficiency of TiO_2 under solar (or visible) light, it is necessary to modify the band-gap of these materials in order to facilitate the visible light absorption. In this respect, the different approach are focused on the introduction of sensitizers as: (i) doping agents, (ii) dyes or (iii) carbonaceous materials [4,5]. The introduction of doping agents into TiO_2 narrows the band gap by producing new hybrid states which confers significant visible light absorbance to TiO_2. On the other hand, the improvement obtained using sensitizers is due to the direct absorption of visible light by the sensitizer and the release of electrons to TiO_2 in an oxidizing reaction.

However, different problems were also detected. Metal doping generates thermal instability, electron trapping by the metal centres and high processing costs [6,7]. Alternatively, doping with non-metals as N and S are used [8,9] being now the main drawbacks (i) the difficulty to obtain high nitrogen concentration; (ii) the formation of defects which can act as recombination centres for carriers [10]; (iii) the decrease of N concentration at the surface layer after irradiation [11].

The incorporation of carbon materials to the photocatalysts improve the TiO_2 photoactivity by different mechanism: (i) carbon absorbs over a wide range of visible light producing band-gap tuning/photosensitization, (ii) minimisation of electron/hole recombination (iii) promotion of the reactants adsorption. The high porosity of material also facilitates (i) the formation of nanoparticles of TiO_2 enhancing the active site number and (ii) the adsorption of pollutants and the contact between reactants and catalysts [12]. Additionally, carbon is a good electron acceptor. Electron transfers to the carbon phase minimize the electron/hole recombination on the TiO_2. Thus, if the particle size is reduced, the distance that the photogenerated electrons and holes need to travel through the

* Corresponding author.
E-mail address: fjmaldon@ugr.es (F.J. Maldonado-Hódar).

http://dx.doi.org/10.1016/j.apcatb.2017.05.090
0926-3373/

surface reaction sites is reduced, thereby reducing the recombination probability.

Together TiO_2, additional metal oxides (ZnO, SnO_2, CeO_2, etc) has proved its photocatalytic efficiency in degrading a wide range of pollutants into biodegradable compounds and eventually mineralizing them to harmless carbon dioxide and water. Among them, the photoactivity of zirconium oxide is associated to its nature as n-type semiconductor, showing a good performance.in the degradation of different pollutants [13–15]. However, photocatalytic activity has not been obtained under visible light, because the high value (5.1 eV) reported for the band-gap energy of this oxide is[16]. Nevertheless, this parameter can be lowered significantly (up to 2.3 eV) depending on the preparation technique, [17] improving in such a manner its potential use as photocatalyst.

ZrO_2 have been used by several authors to increase the photocatalytic activity of TiO_2 [18–21] because the coupling of the two semiconductors can achieve a more efficient charge separation and prolong the lifetime of charge carriers, diminishing significantly the recombination probability between the hole and electron [22,23].

Nevertheless, the combinations of ZrO_2 with carbon materials, and their applications in photocatalysis are less studied. The preparation of C/ZrO_2 composites can result in high performance materials for photocatalytic applications following the same precepts previously described for TiO_2 (high dispersion of the metallic phase, improving porosity, electron transfers, etc). Matsui et al. [24] have prepared nano-sized ZrO_2/carbon clusters composite materials by the calcination of a $ZrOCl_2$/starch complex. These materials show activity under visible light irradiation, when they are pulverized to increase the surface area. They show that the catalytic activity of the pulverized materials increased with the increase of the surface area. Nevertheless, the surface area is low (<100 m^2/g) instead the pulverization process.

In this paper, new ZrO_2-carbon composites were prepared by using a sol–gel process. The flexibility of these processes allows tailoring the physicochemical properties of the composites, and consequently, the optimization of their performance. These new ZrO_2-carbon composites have been tested in the degradation of organic pollutants under visible light. The photocatalytic activity of the composites was evaluated using Orange G as a target molecule, and the relationship of the photocatalytic activity with the physicochemical characteristics of composites was analysed. A high performance of the composites in this reaction under visible light was obtained.

2. Experimental

2.1. Synthesis of ZrO_2-carbon xerogel composites

ZrO_2-carbon xerogel composites were prepared by an one-pot synthesis method using resorcinol-formaldehyde and a zirconium alkoxide as carbon and zirconium oxide precursor, respectively. In a typical synthesis procedure, the proper amount of zirconium propoxide was dissolved in 500 mL of *n*-heptane by stirring (450 rpm) and heated at 70 °C under reflux. Another solution containing resorcinol (R), formaldehyde (F) and water (W) was prepared and added dropwise to the first one. The component molar ratio used in this solution was R/F = 1/2 and R/W = 1/14, while the amount of zirconium alkoxide was fitted according to the final ZrO_2 content desired in the composite. The gel formed was aged at 70 °C for 24 h under stirring after which the suspension was filtered and the solid placed in acetone (2 days, changing acetone twice daily) to exchange water within the pores by acetone, in order to reduce the porosity collapse during the subsequent drying process [25]. Then, the gel was again recovered by filtering and dried by microwave heating using a Saivod MS-287W microwave oven under nitrogen atmosphere in periods of 1 min at 384 W until constant weight. Pyrolysis of ZrO_2-organic xerogel composites to obtain the corresponding ZrO_2-carbon xerogel composites was carried out in N_2 flow at 300 cm^3/min, heating to 900 °C at a heating rate of 1 °C/min, in order to allow a soft removing of pyrolysis gases, and soaking time of 2 h.

ZrO_2-Carbon xerogel composites were refereed as CZrX (X correspond with the theoretical% of ZrO_2 present in the carbonized composite). The theoretical ZrO_2 content and thus, the amount of zirconium propoxide used, was calculated assuming that the R-F polymerization is complete and the weight loss during the carbonization is 50%. Nevertheless, the exact ZrO_2 content of samples was finally determined by thermogravimetric analysis (TGA). TGA was performed in air flow with a heating rate of 10 °C/min using a Mettler-Toledo TGA/DSC1 thermobalance.

To check the influence of the carbonaceous phase on the ZrO_2 crystal structure and physicochemical characteristics of the composite, pure zirconium oxide (Zr100) and carbon phase (C100) were synthesized following the same procedure previously described but without adding the corresponding organic or inorganic precursor. Also, commercial ZrO_2 (from sigma-aldrich) and TiO_2 samples (P25, from Degussa), were used as reference material.

2.2. Characterization

The morphology of supports was studied by scanning electron microscopy (SEM) using a LEO (Carl Zeiss) GEMINI-1530 microscope. Textural characterization was carried out by N_2 and CO_2 adsorption at −196 °C and 0 °C, respectively, using a Quantachrome Autosorb-1 equipment. The BET and Dubinin–Radushkevich equations were applied to determine the apparent surface area (S_{BET}) and the micropore volume (W_0), the mean micropore width (L_0) and the microporous surface (S_{mic}), respectively. Furthermore, the DFT method was used to calculate the mesopore volume of the samples (V_{mes}). Pore size distributions were also obtained by applying the DFT method. The total pore volume was considered as the volume of N_2 adsorbed at $P/P_0 = 0.95$.

The zirconium oxide phase was determined by powder X-ray diffraction (XRD) pattern using a Bruker D8 Advance X-ray diffractometer with Cu Kα radiation at a wavelength (λ) of 1.541 Å. The 2θ angles were scanned from 20 to 70°. The average crystallite sizes (D) were estimated by the Debye-Scherer equation, $D = 0.95\lambda/\beta \cos\theta$, where θ is the diffraction angle and β is the full width at half-maximum (fwhm). The fwhm was determined with an extrapolated baseline between the beginning (low-angle side) and the end (high-angle side) of a diffraction peak with the highest intensity.

Reflectance diffuse analysis of all samples were obtained on a double-beam UV–vis spectrophotometer (CARY 5E from VARIAN) equipped with a Praying Mantis diffuse reflectance accessory (DRA). The reflectance spectra were converted to absorbance by the Kulbelka–Munk (KM) method in order to calculate the band gap (Eg) of samples. Graphic representations were used to calculate Eg: $(F(R)\cdot h\upsilon)^n$ versus E, with n = ½ for an indirect allowed transition and n = 2 for a direct allowed transition. The Eg value was obtained by extrapolating the slope to a = 0 according to the procedure used by López et al. [26].

2.3. Adsorption isotherms and kinetics

The orange G adsorption kinetics on photocatalysts were studied by recording the concentration decay curves in order to calculate the time required to reach the adsorption equilibrium at saturation. These experiments were carried out by placing 0.25 g each sample in contact with 250 mL of Orange G solution (25 ppm) in a flask. This suspension was maintained under shaking in a thermostatic bath at 298 K and aliquots were removed from the reactor

at different times and filtered to determine their orange G concentration. The concentration of Orange G was measured by UV–vis spectrophotometry at 487 nm (5625 Unicam Ltd., Cambridge, UK) in the range indicating a linear relationship between absorbance and concentration. Adsorption kinetics shown the required time to reach the saturation equilibrium of maximum 4 h depending on sample used.

The Orange G adsorption isotherm on CZrX was carried out also in the same thermostatic at 298 K. For this, a volume of 25 mL with different initial concentrations (5–50 mg/L^{-1}) of dye was placed in a flask and 0.025 g of sample was added. The flask was placed inside the thermostatic bath under shaking for 4 h, according to the equilibrium time previously determined in the kinetics experiments.

After reaching equilibrium, the adsorbed amount (q) from experimental data was calculated by following equation:

$$q = \frac{V}{m}(C_0 - C_e)$$

where q is the adsorbed amount (mg/g), V the volume (L) of solution, C_0 the initial Orange G concentration (mg/L), C_e the equilibrium Orange G concentration (mg/L) and m is the amount of adsorbent (g).

Experimental data on the adsorption equilibrium of Orange G were interpreted using the adsorption isotherm models of Langmuir and Freundlich, The Langmuir isotherm is valid for monolayer adsorption onto a surface with a finite number of identical sites. It is given as the following equation:

$$q = \frac{q_m \cdot K_L \cdot C_e}{1 + K_L \cdot C_e}$$

where q is the amount of adsorbate adsorbed per specific amount of adsorbent (mg/g) and C_e is equilibrium concentration (mg/L or mmol/L); q_m is the amount of adsorbate required to form a monolayer (mg/g); K_L is Langmuir equilibrium constant. The linearized form of the Langmuir equation is

$$\frac{C_e}{q} = \frac{1}{q_m K_L} + \frac{C_e}{q_m}$$

q_m and K_L can be determined from the linear plot of C_e/q versus C_e. The values of q_m and K_L calculated from the plots along with the correlation coefficients are listed in Table 4.

On the other hand, the Freundlich isotherm equation is given as below:

$$q = K_F \cdot {C_e}^{1/n}$$

where K_F is the relative adsorption capacity and (1/n) is an indicator of sorption intensity K_F. The linearized form of the Freundlich equation is

$$Lnq = LnK_F + \frac{1}{n}\ln C_e$$

The value of K_F and n can be estimated from the intercept and slope of the linear plot of experimental data of ln q versus ln C_e. The Freundlich isotherm provides no information on the monolayer adsorption density in comparison with the Langmuir model

2.4. Photocatalytic reactor set-up and degradation procedure in presence of saturated photocatalysts

The photocatalytic activity of CZrX composites was compared in the OG degradation using a glass photoreactor (inner diameter of 8.5 cm × height of 20 cm) equipped with an inner tube of 2.5 cm of diameter placed in the reactor centre, allowing to fit a visible lamp of 14 W (ReptoLux 2.0) inside to ensure an uniform irradiation of all solution volume. The degradation kinetic was follow by UV-spectrometry using a UV–vis spectrophotometer (5625 Unicam Ltd., Cambridge, UK), previously calibrated.

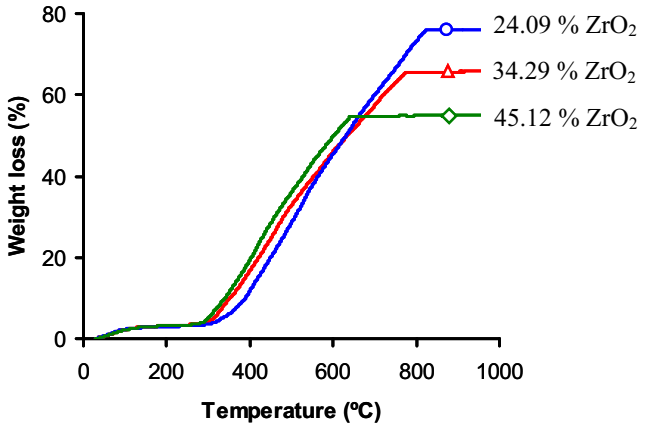

Fig. 1. TGA profiles. CZr20 (●), CZr30 (▲) y CZr40 (◆).

Catalytic photodegradation was carried out using 0.8 g of CZrX composite previously pretreated at 400 °C in H_2 flow for 12 h. Also, before catalytic experiments, all the photocatalysts were saturated with the dye in the dark to avoid the influence of the different adsorptive performance of each sample on the evolution of the dye concentration. This was carried out taking into account the previously results obtained (adsorption capacity and equilibrium time) from the kinetics and isotherms adsorption experiments. After saturation, the initial dye concentration (C_0) was fitted again in all cases to 10 mg/L, and then, visible light was turned on and this time was considered as the start degradation time. At a regular interval of 10 min, equal aliquot was removed from the reactor, filtered and the OG concentration measured by UV-spectrometry. Orange G mineralization degree was followed by the evolution of total organic carbon (TOC) present in the solution during the photo-degradation experience using an analyzer Shimadzu V-CSH analyser with ASI-V autosampler.

Finally, toxicity tests of solutions before and after catalytic degradation were performed using the normalized biotest (UNE/EN/ISO 11345-2) of luminescent inhibition of Vibrio Fischeri bacteria using the LUMIStox 300 system (Dr. LangeGmbH) with a LUMIStherm incubator. Toxicity was expressed as inhibition percentages at 15 min of exposure with reference to a stock saline solution used as control.

3. Results and discussion

3.1. Determination of the zirconium oxide contents in the composites

The fraction of ZrO_2 in the CZrX composites was determined by burning the carbon phase using TGA (Fig. 1). The weight loss between 300 and 800 °C was due to oxidative carbon decomposition. The residual mass, stable after 850 °C was considered as the inorganic solid content. The overall TG residues remaining in the CZr20, CZr30, and CZr40 composites were 24.1 34.3 and 45.1 wt.%, respectively. The mass percentages of zirconia obtained by TGA are lightly higher than the expected ones because the weight loss undergoes by the samples during carbonization also slightly exceed the 50% programmed. The thermal stability of the samples is comparable with those results found in bibliography [27]. It is also noteworthy that all the TG profiles present similar slope, indicating the similar nature of the carbon in all of them.

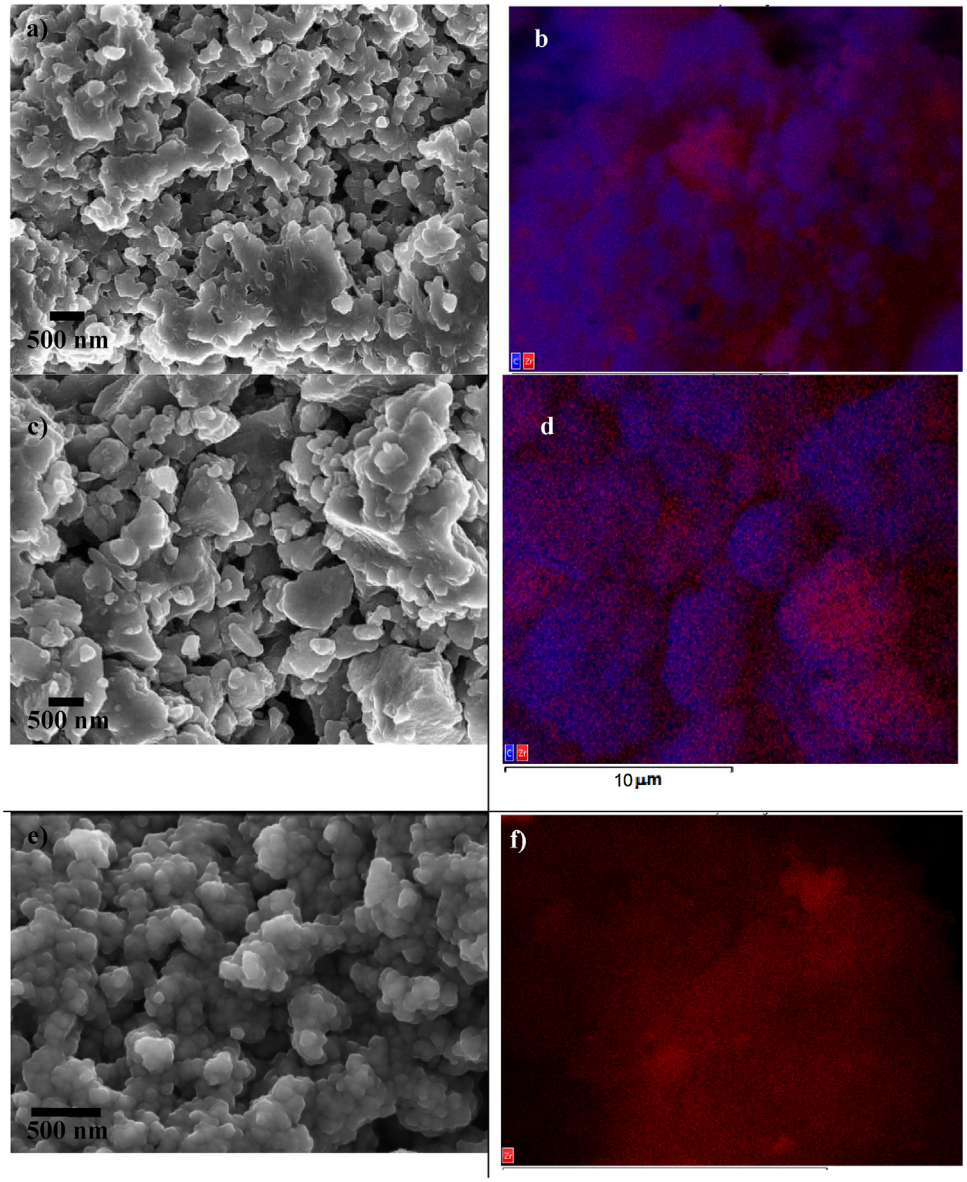

Fig. 2. SEM images showing the morphology and Zr-distribution by EDX mapping in a-b) CZr20, c,d) CZr30 and e,f) CZr40.

3.2. Morphology and ZrO_2 dispersion

The morphology of samples was analysed by scanning electron microscopy and representative images are depicted in Fig. 2(a–c). EDX-mapping was also recorded and shown in Fig. 2(d–f). In sample CZr20 the formation of large and smooth particles is observed, this fact progressively diminish with increasing the ZrO_2 content. Spherical primary particles are progressively more easily identified at the sample surface, although they are highly overlapped in all cases forming a coral-like three-dimensional structure. As consequence, the interparticle voids changes, and a different porous texture is therefore expected in the same way. On the other hand, EDX-mapping shows a homogeneous distribution of ZrO_2 independently of the ZrO_2-content. This fact is in agreement also with the similar thermal stability previously commented.

3.3. Textural characterization

The pore structure of samples was studied by gases adsorption and mercury porosimetry measurements. It is well known that the CO_2 adsorption provides the information about the narrow microporosity, corresponding to micropores with diameter lower than 0.7 nm, while the total microporosity is determined from N_2 isotherm in absence of diffusion restrictions [28]. Both are therefore complementary when studying microporosity. Similarly, while N_2-adsorption permits the characterization of micro and narrow mesopores, mercury porosimetry allows the analysis of the widest mesoporosity and macroporosity. Thus, complementary techniques are used to characterize the complete porosity of samples.

The pore size distributions obtained by mercury porosimetry (Fig. 3) are in clear agreement with the previous morphological changes. Macro and mesopore volumes are collected in Table 1. Although the macropore volume is more or less independent of th the ZrO_2 content of the composite, their PSD change significantly, becoming progressively narrower with increasing the ZrO_2 in such a manner that the formation of mesopores is favoured. Fig. 3 point out that CZr20 is a macroporous solid (without mesopores), with a monomodal macropore size distribution showing a maximum for macropores with a diameter at around 26 µm. With increasing the

Table 1
Textural characteristics of pure phases and CZr composites.

Sample	S_{BET} m^2 g^{-1}	S_{mic} m^2 g^{-1}	W_0 (CO_2) cm^3 g^{-1}	W_0 (N_2) cm^3 g^{-1}	L_0 (N_2) nm	V_{meso} cm^3 g^{-1}	$V_{0.95}$ cm^3 g^{-1}	V_2 cm^3 g^{-1}	V_3 cm^3 g^{-1}
P25	57	n.d.	n.d.	0.006	n.d.	0.080	0.118	n.d.	–
ZrO_2	11	39	0.041	0.002	2.70	0.038	0.040	0.013	1.220
Zr100	11	4	0.013	0.004	2.10	0.057	0.061	n.d.	n.d.
C100	614	952	0.290	0.250	0.78	0.009	0.310	n.d	n.d
CZr20	465	759	0.213	0.182	0.81	0.079	0.261	0.015	1.050
CZr30	418	658	0.183	0.167	0.90	0.261	0.428	0.016	1.320
CZr40	391	582	0.156	0.154	1.05	0.382	0.536	0.125	1.271

*n.d. (not determined).

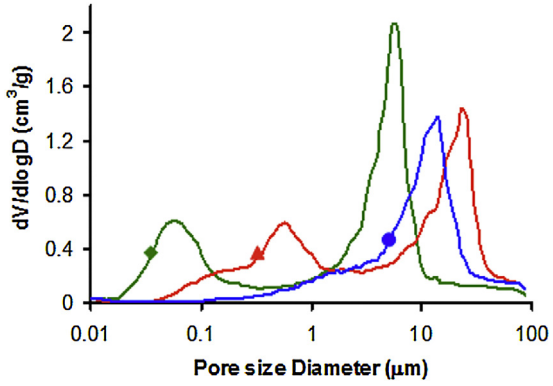

Fig. 3. Pore size distribution PSD obtained by mercury porosimetry. CZr20 (●), CZr30 (▲) y CZr40 (◆).

ZrO_2 content the porosity become narrowest and more heterogeneous. In the case of CZr40 the PSD presents two maxima, the first one includes the mesoporosity range, being centered in pores with a diameter of around 50–60 nm, the second maxima correspond to larger macropores, with a diameter at around 6 μm. It is noteworthy however that even these large macropores are narrower than those detected for CZr20. This bimodal PSD is also observed in the case of CZr30, with present an intermediate behavior between CZr20 and CZr40.

Fig. 4 shows the nitrogen adsorption isotherms of CZr20, CZr30, and CZr40 materials. All isotherms exhibit a mixture of type I and IV isotherm, which is characteristic of micro-mesoporous materials. The shape of the isotherm changes, the slope of the isotherm increase as well the formation of certain hysteresis cycles, but mainly, the N_2-adsorption is favored at high P/P_0 with increasing the ZrO2 content. These facts are indicative of the progressive mesoporosity of samples in this sense as denoted the pore size distribution (PSD) obtained by the BJH method (Fig. 4d). Results obtained from CO_2 and N_2 adsorption are also summarized in Table 1, and shows a great variation of the textural properties between them. The adsorption capacity of both commercial oxides used as reference materials (ZrO_2 and P25) is quite limited, showing in the best case a scarce S_{BET} of 57 m^2/g for P25. The pure inorganic phase Zr100, synthesized in identical conditions that the CZrX composites, also show a very small micropore volume, leading to small values of surface area. On the contrary, the pure carbon phase (C100) presents the higher micropore volume and surface area values.

Thus, the composites become more mesoporous, V_{meso} increases with increasing the ZrO_2 fraction dispersed into the carbon xerogel matrix (Fig. 5a). In this sense, the microporosity becomes also widest (L_0 (N_2) increases) at the expense of the microporosity (W_0 (CO_2)) that decreases (Fig. 5b and c) causing simultaneously the progressive surface area decrease (Fig. 5d). This preparation method enhance the mesoporosity of the composites regarding results previously observed in the bibliography [29,30].

3.4. XRD analyses

Powder XRD measurements of CZr samples were performed in order to identify the crystalline domains of zirconia in each case. Fig. 6 shows the XRD patterns of the CZr composites in comparison with the pure ZrO_2 samples. In these last cases, narrower and intense diffraction peaks were observed in both commercial and Zr100 samples, denoting a high crystallinity. However, diffraction peaks become wider, and the intensity decrease in the case of composites CZrX. Moreover, crystallinity in the composites seems to be more or less independently of the ZrO_2 content, which is in agreement with the homogenous distribution previously observed by EDX-mapping.

The ZrO_2 present three possible crystalline structures: monoclinic, stable at temperatures bellow 1200 °C, tetragonal, stable between 1200 and 2400 °C and cubic, from 2400° to the fusion at around 2680 °C, although is stabilized by different oxides like CaO, MgO or Y_2O_3. The applications of Partially Stabilized Zirconia (PSZ) or Fully Stabilised Zirconia) (FSZ) are well known. In this case, the assignation of the crystallographic phases was carried out according to the bibliography [31–33]. The monoclinic crystalline structure (JCPDS No.37-1484) is observed for the commercial ZrO_2 sample. A mixture of monoclinic (88.9%) and cubic (JCPDS No. 49-1642) phases (11.1%) was obtained for the sample Zr100. The structure of ZrO_2 in the composites is 100% cubic, in spite that all samples were obtained only at 900 °C, where the monoclinic phase should be stabilized. This ratio is obtained according to the ratio of the I_{100} of each phase, corresponding to the peaks at 28.2° and 30.2° for the monoclinic and the cubic phase respectively. These results could be due to the interactions between both organic and inorganic phases, acting in this case the organic phase as a typical ZrO_2 dopant.

It has been reported that the stability of the different crystalline structure of ZrO_2 strongly depends on the crystal size. Jayakumar et al. [34] show the significance of particle size in stabilizing the metastable phases. They observed that the cubic phase could be stabilised at particle size below 6 nm; the tetragonal phase is found to be stable at particle size above 6 nm and below 20 nm and the monoclinic phase is stabilized in large particles (>20 nm). The mean average size of ZrO_2 particles was estimated using the Debye-Scherer equation obtaining sizes of 4.8, 4.7, 4.2, 33.25 and 39.3 nm for CZr20, CZr30, CZr40 composites and C100 and ZrO_2, respectively. This denotes a good dispersion of ZrO_2 nanoparticles in the carbon xerogel framework which can be also related with the stabilization of the cubic phase in composite materials. XRD therefore, confirms that the carbon phase avoid the formation of large ZrO_2 crystallites that remains in the cubic phase after cooling.

3.5. Surface composition: XPS analysis

The chemical characteristics of the catalyst surface were also analyzed by XPS. Some of the results obtained for ZrO_2 characterization are summarized in Tables 2 and 3 , respectively. ZrO2 was used as reference material but even in this case, carbon peaks are

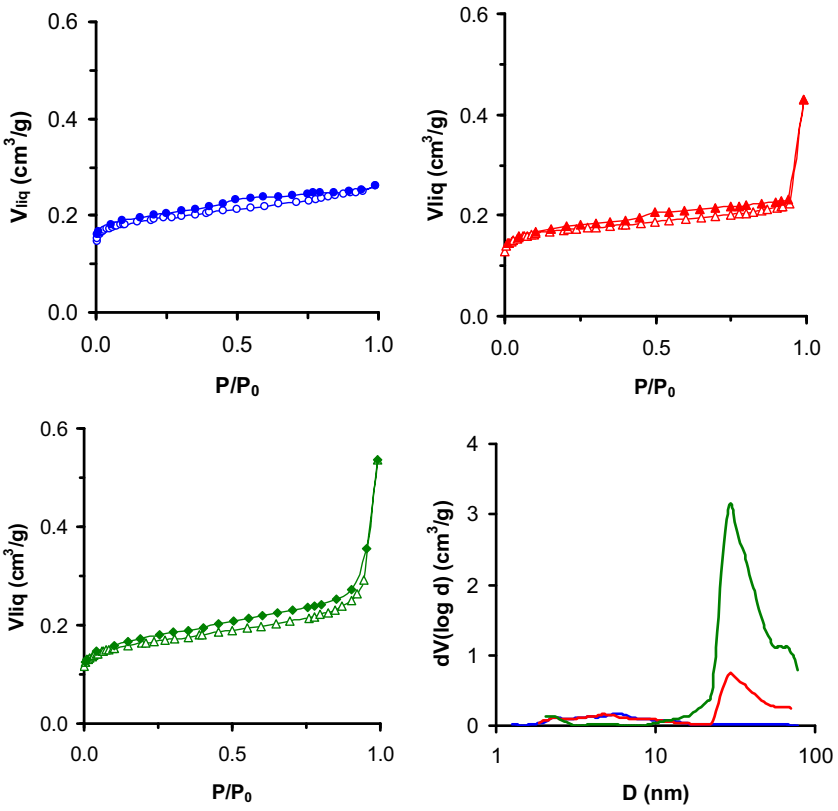

Fig. 4. Nitrogen adsorption-desorption isotherms (a-c), (d) pore size distributions (DFT method). CZr20 (●), CZr30 (▲) y CZr40 (◆).

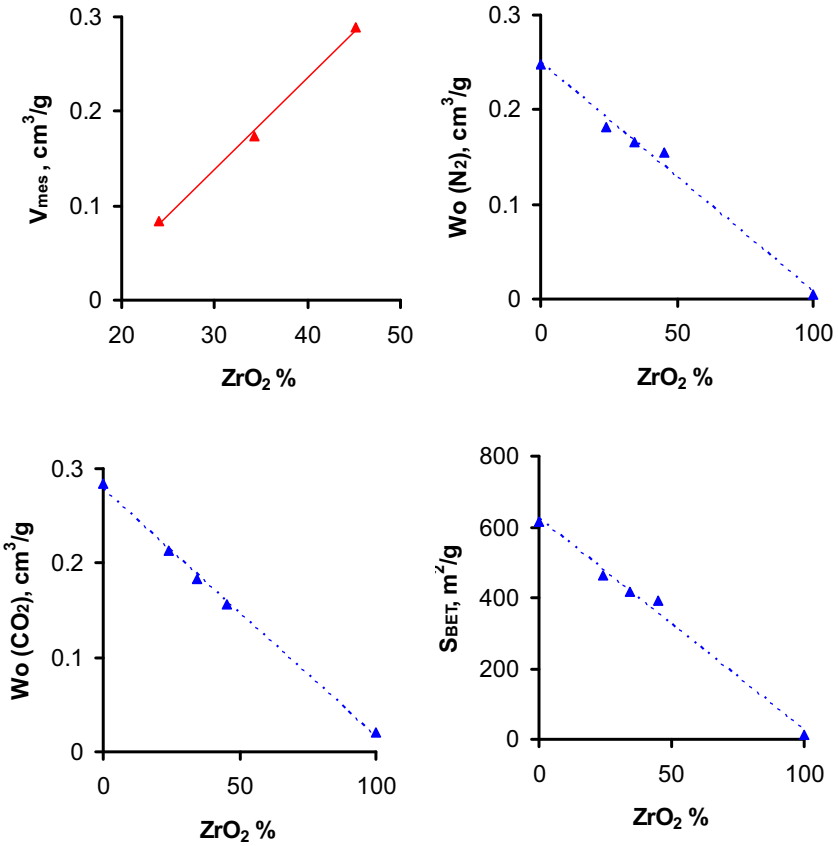

Fig. 5. Influence of ZrO_2 – content on the textural properties of composites.

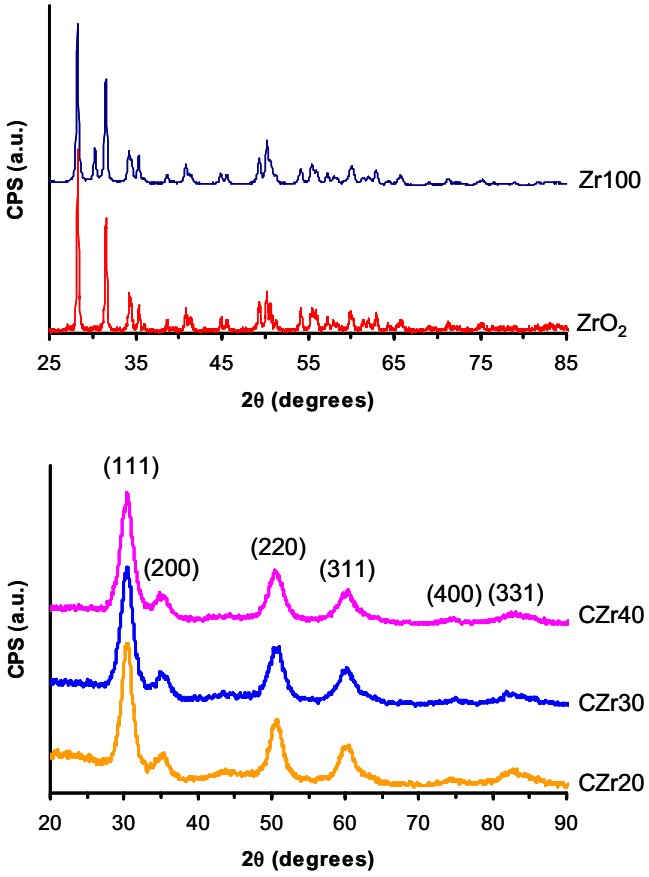

Fig. 6. Powder XRD patterns of samples: a) CZr, b) Zr.

Table 2
Surface composition of composites determined by XPS.

Catalyst	C Wt.%	O Wt.%	Zr Wt.%
ZrO_2	4.2	25.1	70.6
C100	96.4	3.6	0.0
CZr20	88.9	7.2	3.9
CZr30	89.9	5.8	4.3
CZr40	83.3	6.0	10.7

Table 3
XPS results of composite samples: binding energy and percentage of the components used to fit the XPS Zr_{3d}, O_{1s} and C_{1s} spectral regions of CZr photocatalysts.

Catalyst	BE (eV) C_{1s}	Peak%	BE (eV) Zr_{3d}	Peak%	BE (eV) O_{1s}	Peak%
ZrO_2	284.6	71	181.8	73	529.9	78
	286.2	23	182.5	27	531.7	22
	288.9	6				
CZr20	284.6	66	182.3	41	530.4	17
	285.5	17	182.7	43	532.3	59
	286.5	8	183.3	15	533.8	24
	287.4	3				
	289.1	4				
	290.6	1				
CZr30	284.6	67	182.2	44	530.3	21
	285.4	18	182.5	45	532.3	49
	286.5	6	183.2	11	533.9	30
	287.4	4				
	289.1	4				
	290.7	2				
CZr40	284.6	68	182.1	46	530.2	43.9
	285.4	16	182.5	43	532.0	36.8
	286.4	5	183.2	11	533.7	19.3
	287.3	4				
	289.1	3				
	290.6	2				

Table 4
Adsorption isotherm parameters of Orange G on pure oxides and CZr composites at 298 K.

	P25	ZrO_2	CZr20	CZr30	CZr40
Langmuir isotherm					
q_m	3.83	3.01	7.35	16.37	31.69
K_L	0.142	0.023	0.125	0.170	0.665
R^2	0.975	0.900	0.975	0.996	0.999
Freundlich isotherm					
K_F	0.749	0.104	2.325	3.105	11.235
n	2.385	1.378	3.957	2.217	2.701
R^2	0.871	0.957	0.958	0.922	0.919

detected (Table 3) on the surface of Zirconia, which are attributed to adventitious carbon because of sample surface contamination by air and moisture absorption [35,36].

The Zr_{3d} spectral region was analyzed according to the bibliography [37,38]. For the Zr^{+4} in stoichiometric ZrO_2 the Zr $3d_{5/2}$ component is centered at 182 eV. However, three components are required to fit the Zr signal in the composites. For non-stoichiometric oxides (ZrO_y: $0 < y < 2$) the Zr $3d_{5/2}$ band shifted to higher B.E. 182.8 eV [35]. This behaviour is observed clearly in all the composite samples (Fig. 7), with a sifthening of about 0.5 eV and the formation of different suboxides. The surface composition of the samples is summarized in Table 2. The Zr and O contents do not increase proportionally to the inorganic ratio in the composite. Moreover, the ZrO_2 content in surface (detected by XPS) is significantly smaller than in the bulk of the composite (detected by TG). This fact can be consequence of the different crystal structure of pure ZrO_2 and ZrO_2 in the composites, a certain crystal growth or to the encapsulation

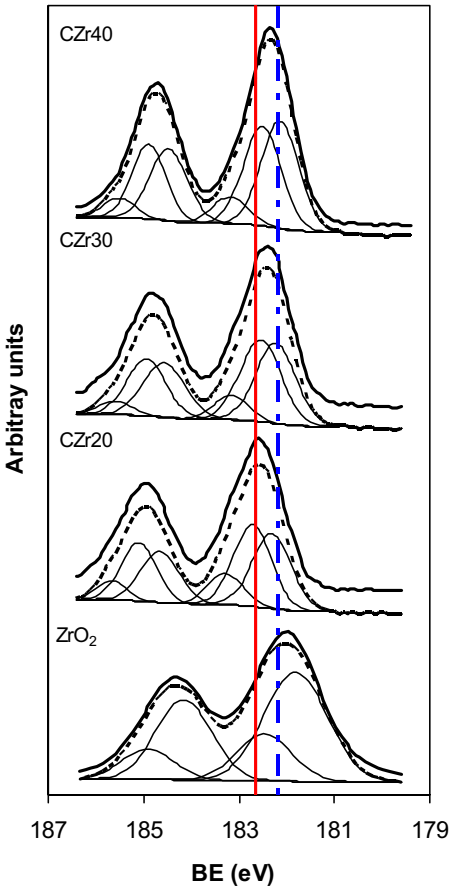

Fig. 7. Survey and deconvolution of the Zr_{3d} spectral region. Dashed line: Zr^{+4} Continuous line: non-stoichiometric oxides, ZrO_y: $0 < y < 2$.

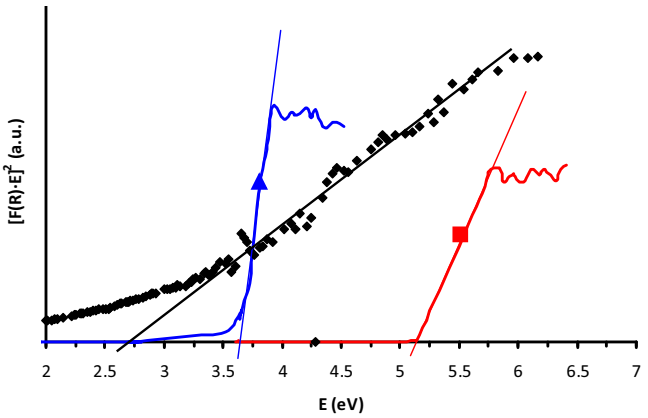

Fig. 8. Diffuse reflectance spectra of P25 (▲), ZrO_2 (■) and CZr40 (♦).

of ZrO_2 nanoparticles by the carbon phase, which can be in agreement with the intimate interactions between the phases needed to the doping character of the carbon phase previously showed. This is also confirmed by the significant increase of suboxides proportion in the composites with the formation of a third component at 183.2 eV. Nevertheless, the proportion of the different Zr components in the different composites are quite similar between then, denoting again that in all cases the inorganic nanoparticles can present similar nature and dispersion.

A similar behaviour can be described for the O_{1s} region. The O_{1s} component associated to the Zr–O–Zr appears at 530.2 eV [39]. Additional components correspond to the formation of oxygenated surface groups like Zr—O—H (531.8 eV) or physisorbed water H—O—H (532.7 eV). For pure carbon phases, the O1s spectrum shows typically two components at 532.0 eV due to double C=O bonds from ketones and carboxylic acids, and at 533.9 eV due to single C—O bonds from alcohols, phenols and carboxylic acids [40].

For ZrO_2 the major component of O_{1s} spectral region corresponds to the 'bulk' oxygen atom in the stoichiometric ZrO_2 form, the second peak associated to the hydroxyl groups, as commented. In the composites, clearly the O1s of Zr-O-Zr is also shifted to higher B.E. (between 0.4–0.5 eV higher). The second peak in this case can present also the contribution of surface groups on the inorganic phase as the C=O component of the carbon phase. Nevertheless, the last peak is clearly due to the C—O bonds. Moreover, this assignation is confirmed by the fact that the first component increases progressively with increasing the Zr-content in the composite.

3.6. Diffuse reflectance analysis

Diffuse reflectance spectra were recorded in order to calculate the band gap (Eg) of samples. We studied the electronic properties of the materials according to the Kubelka–Munk theory. According to this authors, it is possible to determine Eg by plotting $(F(R)\cdot h\upsilon)^2$ against $h\upsilon$ (Fig. 8). The sample P25 was used as reference materials. The Eg determined for this sample was 3.61 eV, in agreement with the values described in the bibliography [41,42]. The calculated band gaps for pure ZrO_2 is 5.12 eV, and a slight decrease of band-gap is observed for composites with increasing the ZrO_2 content (2.75, 2.65 and 2.50 for CZr20, CZr30 and CZr40, respectively).

The CZr samples show smaller band gap as compared with the pure ZrO_2 as well as, compared with pure TiO_2. This Eg values obtained from diffuse reflectance spectra results show that the CZr samples could present a high potential as photocatalyst working under the visible radiation, while this behaviour is not expected for ZrO_2 samples due to its high band gap. This redshift in CZr samples band gap could be due to the quantum confinement experienced by the well dispersed ZrO_2 on the carbon matrix [43]. Also, the presence of new zirconium states detected by xps in the band gap could narrows the band gap and confers significant visible light absorbance to ZrO_2.

3.7. Adsorption equilibrium studies

The adsorption isotherms of Orange G were fitted by using the models of Langmuir and Freundlich. Results are shown in Table 4. In general, higher correlations were obtained by applying the Langmuir equation regarding the Freundlich one. Differences are greater with increasing the ZrO_2-content in the composite, denoting the influence of the textural transformation previously discussed. Fig. 9b shows the amount of adsorbate required to form a monolayer (q_m) as a function of the adsorbent mesopores volume. A linear relationship could be observed between both which denotes a preferential adsorption of Orange G on the adsorbent mesoporosity. Due to the kinetic size of Orange G (x = 5.44 A, Y = 10.14 A and Z = 15.67A) [44] and the narrow micropores size on CZr samples (<10 A), micropores does not play an important contribution in the Orange G adsorption.

3.8. Photocatalytic activity

To investigate the photocatalytic activity of CZrX composites, the degradation of Orange G (Fig. 10a) was carried out using an artificial visible light. Pure ZrO_2, carbon (C100) and P25 were used as reference materials. As can be seen, no degradation has been observed without using catalyst (photolysis) nor using carbon or

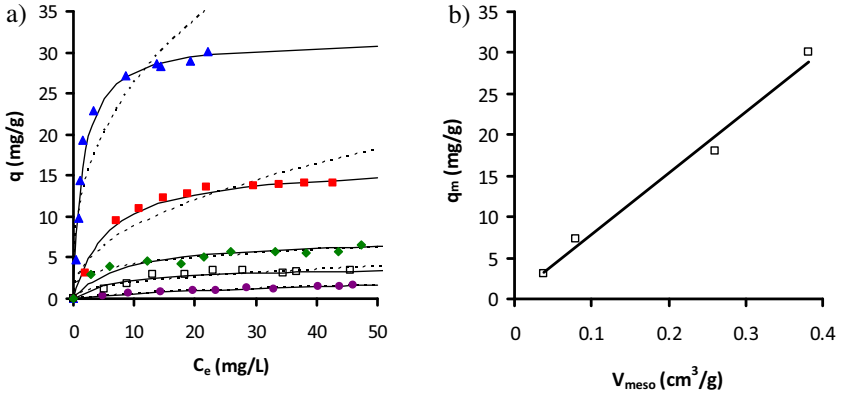

Fig. 9. a) Adsorption isotherms of Orange G on P25 (□), ZrO_2 (●) and composites samples: CZr20 (◆), CZr30 (■) and CZr40 (▲). Dashed line: Freunlich fitting and continuous line: Langmuir fittings. b) Influence of the mesopore volume on the dye adsorption capacity of the samples.

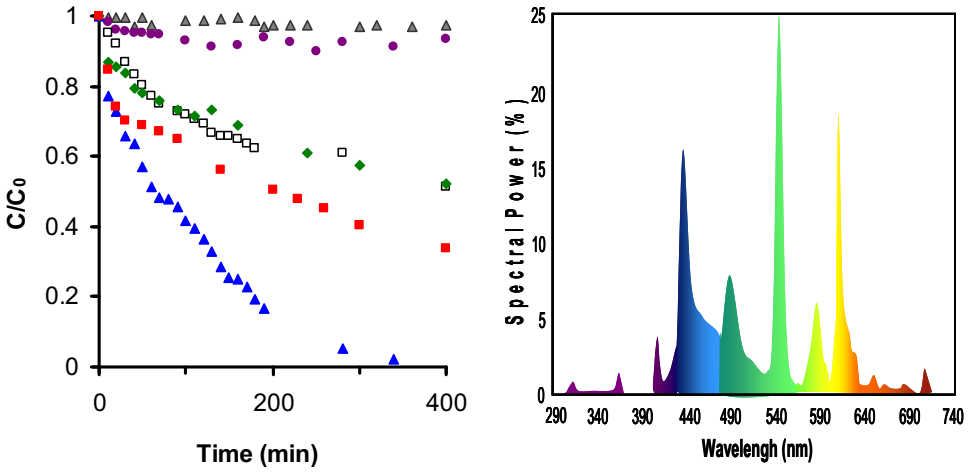

Fig. 10. Left: Kinetic of Orange G photocatalytic degradation and Right: lamp emission spectrum. Zr100 (●), A8 (△), P25 (□), ZrC20 (◆), ZrC30 (■) and ZrC40 (▲). (For interpretation of the references to colour in this figure legend, the reader is referred to the web version of this article.)

ZrO_2 samples. The OG degradation at 6 h of reaction using the commercial P25 catalysts was 43.5%. These results were significantly improved for composites, obtaining a degradation of 47.7%, 63.0% and 98.0% for CZr20, CZr30 and CZr40, respectively.

CZrX composites are more efficient than the pure samples even at low ZrO_2–content on the composite. These data shown that there is a very high synergic effect between carbon xerogel and ZrO_2 improving the photoactivity of the pure samples and, what is more important, turning them into active catalysts under visible light even instead the low lamp power (14 W).

These results are related with the band gap of samples considering the emission spectrum of the visible lamp used (Fig. 10b). It can be observed that no emission energy appears at 5.1 eV (ZrO_2 band gap) or higher energy, so that, electron could not promote from the valence band to the conduction one on ZrO_2 sample and consequently, no degradation is observed. However, a 2% of the radiation spectrum has a higher energy than the P25 band gap allowing degradation reaction using this sample. Due to the lowest band gap of CZr materials, the higher photocatalytic activity of these materials on the visible range can be also assigned to its higher absorption in this region (higher amount of the radiation spectrum is used for degradation reactions), increasing the photocatalytic activity.

The photocatalytic activity of ZrO_2 under UV radiation has been proved by different authors and has been attributed to the structural defects. Yu et al. have synthesized $Ti_{1-x}Zr_xO_2$ with a higher photocatalytic activity than pure anatase TiO_2. The increase in activity is related to the changes in the lattice parameters caused by zirconium substitution. It is proposed that the lattice O^{2-} and O^- ionosorbed on surface are responsible for the increased photoactivity [45]. Wang et al. [46] correlated especially surface properties such as surface area, surface acidity and surface defects with the ZrO_2 photocatalytic efficiency. Ashok et al. [47] investigated the role of oxygen vacancies in ZrO_2 which enhances photocatalytic activity. However, not activity of ZrO_2 has been reported before under visible light.

The extremely high Orange G removal efficiency under visible light observed in carbon composite materials could be attributed to the influence of the carbon support on the characteristics of the ZrO_2 active phase. Due to the good dispersion and contacts between the carbon matrix and ZrO_2 nanoparticles, the flow of propagated electrons amidst the carbon matrix and conduction band of ZrO_2 is increased. Electron transfer between carbon – ZrO_2 phases were previously pointed out by variation on the BE of the species in the composites regarding pure phases, as well the formation of non-stoichiometric phases and the stabilization of the cubic crystalline structure. This synergistic effect between these components effectively reduces the recombination of electron-holes leading to the increased charge carrier separation. These properties enable the Orange G removal under visible light.

The formation of the oxygen vacancies and intermediate electronic states located between the valence and the conduction bands reduced the band gap of the samples and is responsible of the appearance of the visible light photocatalytic activity due to a new photoexcitation process [48]. The stabilization of the cubic zirconia phase could play an important role in the band gap shifting. The band gap for the different zirconia phase has been calculated by different authors [49–51]. All these authors obtained lower band gap energy in the sense cubic < tetragonal < monoclinic phase. Zandiehnadem and Murray [51] studied zirconia in the cubic, tetragonal and monoclinic phases obtaining the band gaps of 3.84, 4.11 and 4.51 eV, respectively, for the three phases. Bechepeche et al. [50] obtained a band gaps of 2.88, 3.05 and 5.25 eV for cubic, tetragonal and monoclinic phases which agrees with the experimental band gap obtained by diffuse reflectance (5.12 eV for monoclinic zirconia). As consequence, the lower band gaps obtained for composite materials could be also related with the stabilization of cubic phase produced by the carbon matrix in these materials and so, the visible photoactivity observed. In these sense, comparing the activity of Zr100 and ZrO_2 samples in the photodegradation of the Orange G it is observed that no degradation activity is observed using ZrO_2 sample where monoclinic phase is present, while around 7% of degradation is obtained using Zr100 where a mixture of cubic (11.1%) and monoclinic (88.9%) is observed by XRD (Fig. 6).

Nevertheless, the key of the efficiency of the catalytic degradation is the degree of mineralization of the pollutant, because intermediates can be even more dangerous than the proper pollutant. Mineralization was assessed by measuring the variation of the total organic carbon (TOC) concentration as a function of irradiation time (Fig. 11, open symbols). As observed, the percentage TOC mineralization is similar to the percentage of Orange G degradation for the same irradiation times, indicating that Orange G is completely mineralized. Also, toxicity tests was performed (Fig. 11, lines) showing a closed behaviour to the TOC and degradation curve at same irradiation times. This fact indicates that photodegradation of Orange G is complete to CO_2, reducing simultaneously the toxicity of the treated water.

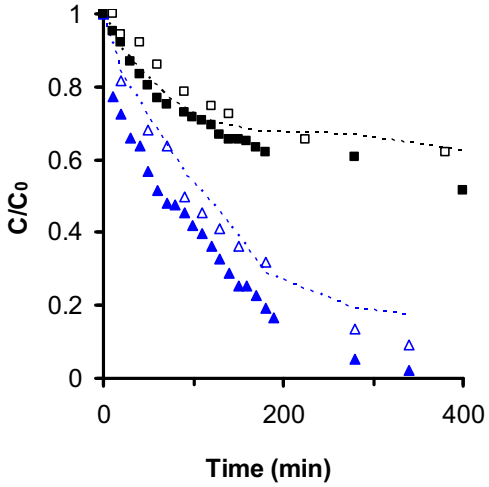

Fig. 11. a) open symbols: TOC/TOC$_0$, close symbols: C/C$_0$, line: Inhibition/Inhibition$_0$. ▲ ZrC40, ■ P25.

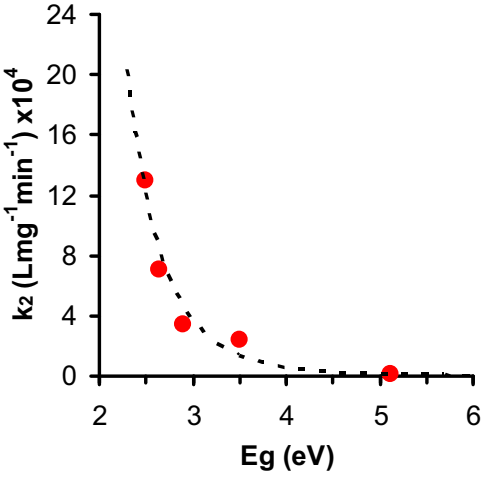

Fig. 12. XXX.

Table 5
Summary of visible light photodegradation of Orange G on different solids at given initial concentration of Orange G (C$_0$ = 10 mg/L).

Catalyst	k_1 (min^{-1})	R^2	k_2 ($L\,mg^{-1}\,min^{-1}$)	R2	S
P25	3.2×10^{-3}	0.912	2.4×10^{-4}	0.955	–
Zr100	5.4×10^{-4}	0.436	1.0×10^{-5}	0.896	–
CZr20	2.3×10^{-3}	0.509	3.4×10^{-4}	0.942	16
CZr30	3.1×10^{-3}	0.739	7.1×10^{-4}	0.934	47
CZr40	9.1×10^{-3}	0.900	1.3×10^{-3}	0.956	130

3.9. Photocatalysis kinetic studies

The photocatalytic degradation processes were fitted by the first order, and second-order kinetics given by the following equations, respectively:

$$r = -\frac{dC}{dt} = k_1 C \rightarrow \mathrm{Ln}\frac{C}{C_0} = -k_1 t \rightarrow C = C_0 \cdot \exp(-k_1 t)$$

$$r = -\frac{dC}{dt} = k_2 C^2 \rightarrow \frac{1}{C/C_0} = k_2 C_0 t + 1$$

where r is the rate of Orange G degradation ($mg\,L^{-1}\,min^{-1}$), C the concentration at any time (mg/L), k_1 the first-order rate constant (min^{-1}) and k_2 the second-order rate constant ($L\,mg^{-1}\,min^{-1}$). Data shows that second order kinetic adjust better the results (Table 5), so, the activity of the prepared catalysts can be evaluated by comparing the apparent second-order rate constants (k_2) listed in Table 2. Second order kinetics are ploted versus Eg in Fig. 12. An exponential increase of the degradation rate of orange G is obtained decreasing the band-gap.

A synergy factor (S) is defined as S = k_2(CZrX)/k_2(Zr100) to quantify the synergetic effect [52]. The introduction of 20% of ZrO_2 into carbon matrix obviously creates a kinetic synergetic effect in Orange G degradation with an increase in the rate constant by a factor of 16. The best result is obtained using the CZr40 where the synergic factor is a very high value of 160.

4. Conclusions

Carbon xerogel-ZrO_2 composites (CZrX) were successfully synthesized through an one-pot sol-gel synthesis. The XRD results confirm the presence of well dispersed (< 4.5 nm) cubic ZrO_2 on the carbon support, homogeneously distributed on the carbon surface, as pointed out the SEM-EDX mapping. Gas adsorption and mercury porosimetry measurement pointed out that the increase of ZrO_2 in the carbon matrix produces an increase in the mesopore volume as well as a widening of the microporosity. The band gaps of the CZrX samples are lower than 2.8 eV making then an excellent photocatalysts under visible light. In this sense, CZrX samples were used for the photocatalytic degradation of Orange G. Due to the synergetic effect between organic-inorganic phases, CZrX efficiency is higher even than TiO2 (P25), providing an effective and faster degradation of Orange G. This best behaviour could be related with the role of carbonaceous materials in different aspects of the composites: i) stabilizing the cubic phase which have a lower band gap, reducing the band gap of samples, ii) favouring the dispersion of zirconia nanoparticles, thus reducing the distance that the photogenerated electrons and holes need to travel, thereby reducing the recombination probability iii) favouring the electron transfers between carbon and ZrO_2 phases (as is shown by XPS), reducing in such a manner the charge carriers recombination and iv) favouring the formation of non-stoichiometric ZrOx oxides, increasing the oxygen vacancies which produce new hybrid states in the band gap, which narrows the band gap and confer significant visible light absorbance.

Acknowledgements

EBG acknowledges for a pre-doctoral fellowship to the project CTM2010-18889. This research is supported by the FEDER and Spanish projects CTQ2013-44789-R (MINECO) and P12-RNM-2892 (Junta de Andalucía).

References

[1] A. Mills, S. Le Hunte, J. Photochem. Photobiol. A: Chem. 108 (1997) 1–35.
[2] M. Pelaez, N.T. Nolan, S.C. Pillai, M.K. Seery, P. Falaras, A.G. Kontos, P.S.M. Dunlop, J.W.J. Hamilton, J.A. Byrne, K. O'Shea, M.H. Entezari, D.D. Dionysiou, Appl. Catal. B: Environ. 125 (2012) 331–349.
[3] W. Ren, Z. Ai, F. Jia, L. Zhang, X. Fan, Z. Zou, Appl. Catal. B: Environ. 69 (2007) 138–144.
[4] J. Zhang, Y. Wu, M. Xing, S.A.K. Leghari, S. Sajjad, Energy Environ. Sci. 3 (2010) 715–726.
[5] S. Lee, Y. Lee, D.H. Kim, J.H. Moon, ACS Appl. Mater. Interfaces 5 (2013) 12526–12532.
[6] Y. Wang, H. Cheng, Y. Hao, J. Ma, W. Li, S. Cai, Thin Solid Films 349 (1999) 120–125.
[7] H. Yamashita, M. Honda, M. Harada, Y. Ichihashi, M. Anpo, T. Hirao, N. Itoh, N. Iwamoto, J. Phys. Chem. B 102 (1998) 10707–10711.
[8] Y. Izumi, T. Itoi, S. Peng, K. Oka, Y. Shibata, J. Phys. Chem. C 113 (2009) 6706–6718.
[9] C. Di Valentin, E. Finazzi, G. Pacchioni, A. Selloni, S. Livraghi, M.C. Paganini, E. Giamello, Chem. Phys. 339 (2007) 44–56.
[10] H. Irie, Y. Watanabe, K. Hashimoto, J. Phys. Chem. B 107 (2003) 5483–5486.

[11] M. Kitano, K. Funatsu, M. Matsuoka, M. Ueshima, M. Anpo, J. Phys. Chem. B 110 (2006) 25266–25272.
[12] R. Leary, A. Westwood, Carbon 49 (2011) 741–772.
[13] S.G. Botta, J.A. Navío, M.C. Hidalgo, G.M. Restrepo, M.I. Litter, J. Photochem. Photobiol. A: Chem. 129 (1999) 89–99.
[14] M. Alvarez, T. López, J.A. Odriozola, M.A. Centeno, M.I. Domínguez, M. Montes, P. Quintana, D.H. Aguilar, R.D. González, Appl. Catal. B: Environ. 73 (2007) 34–41.
[15] C. Karunakaran, S. Senthilvelan, J. Mol. Catal. A: Chem. 233 (2005) 1–8.
[16] S. Polisetti, P.A. Deshpande, G. Madras, Ind. Eng. Chem. Res. 50 (2011) 12915–12924.
[17] B. Králik, E.K. Chang, S.G. Louie, Phys. Rev. B 57 (1998) 7027–7036.
[18] N. Binitha, Z. Yaakob, R. Resmi, Cent. Eur. J. Chem. 8 (2010) 182–187.
[19] D. Zhang, F. Zeng, Appl. Surf. Sci. 257 (2010) 867–871.
[20] X. Fu, L.A. Clark, Q. Yang, M.A. Anderson, Environ. Sci. Technol. 30 (1996) 647–653.
[21] V. Vishwanathan, H.S. Roh, J.W. Kim, K.W. Jun, Catal. Lett. 96 (2004) 23–28.
[22] B. Jiang, S. Zhang, X. Guo, B. Jin, Y. Tian, Appl. Surf. Sci. 255 (2009) 5975–5978.
[23] R. Zheng, X. Meng, F. Tang, Appl. Surf. Sci. 255 (2009) 5989–5994.
[24] H. Matsui, N. Ohkura, S. Karuppuchamy, M. Yoshihara, Ceram. Int. 39 (2013) 5827–5831.
[25] E. Gallegos-Suárez, A.F. Pérez-Cadenas, F.J. Maldonado-Hódar, F. Carrasco-Marín, Chem. Eng. J. 181–182 (2012) 851–855.
[26] R. López, R. Gómez, J. Sol-Gel Sci. Technol. 61 (2012) 1–7.
[27] J.M. Oh, A.S. Kumbhar, O. Geiculescu, S.E. Creager, Langmuir 28 (2012) 3259–3270.
[28] D. Cazorla-Amorós, J. Alcañiz-Monge, A. Linares-Solano, Langmuir 12 (1996) 2820–2824.
[29] J.M. Oh, A.S. Kumbhar, O. Geiculescu, S.E. Creager, Langmuir 28 (2012) 3259–3270.
[30] X.R. Chen, Y.H. Ju, C.Y. Mou, J. Phys. Chem. C 111 (2007) 18731–18737.
[31] R. Srinivasan, R.J. De Angelis, G. Ice, B.H. Davis, J. Mater. Res. 6 (1991) 1287–1292.
[32] D.G. Lamas, A.M. Rosso, M.S. Anzorena, A. Fernández, M.G. Bellino, M.D. Cabezas, N.E. Walsöe de Reca, A.F. Craievich, Scripta Mater. 55 (2006) 553–556.
[33] D.G. Lamas, R.O. Fuentes, I.O. Fábregas, M.E. Fernández de Rapp, G.E. Lascalea, J.R. Casanova, N.E. Walsöe de Reca, A.F. Craievich, J. Appl. Cryst. 38 (2005) 867–873.
[34] S. Jayakumar, P.V. Ananthapadmanabhan, T.K. Thiyagarajan, K. Perumal, S.C. Mishra, G. Suresh, L.T. Su, A.I.Y. Tok, Mater. Chem. Phys. 140 (2013) 176–182.
[35] J.F. Liu, C. Nistorica, I. Gory, G. Skidmore, F.M. Mantiziba, B.E. Gnade, Thin Solid Films 492 (2005) 6–12.
[36] W. He, Z. Guo, Y. Pu, L. Yan, W. Si, Appl. Phys. Lett. 85 (2004) 896–898.
[37] J. Park, J.K. Heo, Y.-C. Kang, Bull. Korean Chem. Soc. 31 (2010) 397.
[38] W.-J. Qi, R. Nieh, B. Hun Lee, L. Kang, Y. Jeon, J.C. Lee, Appl. Phys. Lett. 77 (2000) 3269.
[39] Y. Mi, J. Wang, Z. Yang, Z. Wang, H. Wang, S. Yang, RSC Adv. 4 (2014) 6060–6067.
[40] J.F. Vivo-Vilches, E. Bailón-García, A.F. Pérez-Cadenas, F. Carrasco-Marín, F.J. Maldonado-Hódar, Carbon 68 (2014) 520–530.
[41] M. Anpo, P.V. Kamat, Environmentally Benign Photocatalysts: Applications of Titanium Oxide-based Materials, Springer, New York, 2010.
[42] R. López, R. Gómez, J. Sol-Gel Sci. Technol. 61 (2012) 1–7.
[43] N.L. Zhang, Z.T. Song, Q. Wan, Q.W. Shen, C.L. Lin, Appl. Surf. Sci. 202 (2002) 126–130.
[44] X. Zhao, X. Bu, T. Wu, S.T. Zheng, L. Wang, P. Feng, Nat. Commun. 4 (2013) 1–9.
[45] J.C. Yu, J. Lin, R.W.M. Kwok, J. Phys. Chem. B 102 (1998) 5094–5098.
[46] X. Wang, Q. Zhang, Q. Wan, G. Dai, C. Zhou, B. Zou, J. Phys. Chem. C 115 (2011) 2769–2775.
[47] A.B. Nawale, N.S. Kanhe, S.V. Bhoraskar, V.L. Mathe, A.K. Das, Mater. Res. Bull. 47 (2012) 3432–3439.
[48] I. Nakamura, N. Negishi, S. Kutsuna, T. Ihara, S. Sugihara, K. Takeuchi, J. Mol. Catal. A: Chem. 161 (2000) 205–212.
[49] E.V. Stefanovich, A.L. Shluger, C.R.A. Catlow, Phys. Rev. B 49 (1994) 11560–11571.
[50] A.P. Bechepeche, O. Treu, E. Longo, C.O. Paiva-Santos, J.A. Varela, J. Mater. Sci. 34 (1999) 2751–2756.
[51] F. Zandiehnadem, R.A. Murray, W.Y. Ching, Physica B + C 150 (1988) 19–24.
[52] W. Wang, P. Serp, P. Kalck, J.L.s. Faria, J. Mol. Catal. A: Chem. 235 (2005) 194–199.